Energy Technology
Generation, Conversion, Storage, Distribution
www.entechnol.de

Silver Thiophosphate (Ag_3PS_4) as a Multielectron Reaction Active Material for Lithium Solid-State Batteries

*Zhenggang Zhang, Rongbin Wang, Katherine A. Mazzio, Norbert Koch, and Philipp Adelhelm**

Beyond its Li-ion conductivity, the solid electrolyte lithium thiophosphate (β-Li_3PS_4) exhibits redox activity when its electrochemical stability window is exceeded. As this redox activity can be (partially) reversible, thiophosphates may be used as cathode active materials (CAM). Silver thiophosphate (Ag_3PS_4) is a well-known Ag-ion conductor, which has the same crystal structure and similar chemical composition as β-Li_3PS_4. Here, Ag_3PS_4 is selected and studied as the CAM for Li solid-state batteries (Li-SSBs) with the configuration (In/InLi| β-Li_3PS_4| Ag_3PS_4: β-Li_3PS_4: C65 = 40: 50: 10 wt%). The cells provide a discharge capacity of 325 mAh g^{-1} at 10 mA g^{-1}, but suffer from continuous capacity fading during cycling with an average Coulomb efficiency of 97% at 50 mA g^{-1}. The reaction mechanism is studied using X-ray diffraction, X-ray photoelectron spectroscopy, Raman spectroscopy, and impedance spectroscopy. Overall, the reaction of Li with Ag_3PS_4 is found to be initially partially reversible, but over cycling Ag_2S and S_8 become the active materials along with the formation of other byproducts such as $Ag_2P_2S_6$ and $Li_2P_2S_6$.

1. Introduction

Solid-state batteries (SSBs) are considered as one of the most promising alternatives to lithium ion batteries (LIBs) as they may provide a higher energy density combined with improved safety.[1,2] Compared to conventional liquid electrolyte LIBs, the use of a solid electrolyte (SE) in SSBs also presents new challenges as mechanical properties become even more important. Furthermore, the complex interplay between the various (electro-)chemical and mechanical properties of the anode, cathode, and SE has so far limited the commercialization of SSBs that operate at room temperature.[3] Hence, SEs with moderate stiffness, fast ionic conductivity, and stable (electro) chemical properties are prerequisites for SSBs. Sulfide solid electrolytes (SSEs), such as β-Li_3PS_4, are therefore widely considered for application in SSBs thanks to their high ionic conductivity and moderate stiffness relative to oxide and polymer SEs.[4–6] However, side reactions are known to occur in batteries that utilize SSEs that can often be attributed to their narrow ESW.[7] This situation becomes worse in cases where high operating voltages are required, such as when using NCM811 or lithium-rich layered oxides. Interestingly, studies have also shown that the side reactions arising from SSEs generally involve both sulfur and phosphorous. Pristine Li_3PS_4 oxidizes to elemental sulfur and compounds with P–$[S]_x$–P type interconnected networks, such as $Li_4P_2S_8$, $Li_4P_2S_7$, and $Li_2P_2S_6$, while reduction of Li_3PS_4 leads to $Li_4P_2S_6$, Li_3P, and Li_2S. These redox processes can be partially reversible.[8–11] After decomposition of the SE, the underlying storage mechanisms typically rely on a conversion reaction with sulfur or phosphorous as the redox active components. While these reactions are generally undesired, they may provide additional capacity to the cell. In extreme cases, Li_3PS_4 can also act as an active electrode material in SSBs when ball-milled with a carbon additive, as reported by Hakari et al.[12] A capacity enhancement of the SSB due to a (partially) reversible redox activity of the SE has been found for several frequently used SEs. The additional capacity typically comes with the drawback of increasing cell resistance and hence poor cycle life.[8,11,13–15] On the other hand, choosing compounds as active materials that are chemically and structurally similar to Li_3PS_4 may be attractive for the design of SSBs with overall more compatible chemo-mechanical properties.

Z. Zhang, K. A. Mazzio, P. Adelhelm
Institut für Chemie
Humboldt-Universität zu Berlin
Brook-Taylor-Str. 2, 12489 Berlin, Germany
E-mail: philipp.adelhelm@hu-berlin.de

Z. Zhang
The European Synchrotron Radiation Facility
71 Avenue des Martyrs, 38000 Grenoble, France

R. Wang, N. Koch
Institut für Physik
Humboldt-Universität zu Berlin
Brook-Taylor-Str. 6, 12489 Berlin, Germany

K. A. Mazzio, N. Koch, P. Adelhelm
Helmholtz-Zentrum Berlin für Materialien und Energie GmbH,
Research Groups Operando Battery Analysis (CE-GOBA) and
Hybride Material Systems
Hahn-Meitner-Platz 1, 14109 Berlin, Germany

N. Koch, P. Adelhelm
Center for the Science of Materials Berlin (CSMB)
Humboldt-Universität zu Berlin
Zum Großen Windkanal 2, 12489 Berlin, Germany

The ORCID identification number(s) for the author(s) of this article can be found under https://doi.org/10.1002/ente.202401040.

DOI: 10.1002/ente.202401040

As an example, ternary transition-metal thiophosphates (TM_xPS_y, where TM: Fe,[16] Ni, Co, Ag, Cu,[17,18] etc.) could have better compatibility with β-Li_3PS_4 than other compounds due to their structural and chemical similarities,[19] but they have rarely been studied in SSBs. $FePS_3$ was the first ternary thiophosphate investigated in SSBs, but these experiments focused exclusively on its intercalation properties, and it demonstrated a gradual capacity fading over time.[16,20] We later studied Cu_3PS_4 as an active material, which demonstrated high capacities in both lithium SSBs and sodium ion batteries with liquid electrolytes.[17,18] Ag_3PS_4 is a ternary transition metal thiophosphate that is a well-known silver ionic conductor whose Ag^+ conductivity can reach up to 8.5×10^{-4} S cm^{-1} at room temperature.[21] Meanwhile, the lower electronegativity of Li vs. Ag indicates that a reaction between Li and Ag_3PS_4 is thermodynamically favorable. Ideally, without considering the alloying of Li with Ag below 0.8 V vs. Li^+/Li,[22] the multielectron reaction between Ag_3PS_4 and Li is expected to follow Equation (1).

$$Ag_3PS_4 + 11Li \rightleftharpoons 3Ag + Li_3P + 4Li_2S \quad (1)$$

Based on the reaction in Equation (1), Ag_3PS_4 can be calculated to have a theoretical capacity of 610 mAh g^{-1}, making it a potential high-capacity electrode. It is worth pointing out that the mixed ion and electron conductor Ag_2S could be one possible intermediate product during cycling, considering the formation of Cu_2S in the case of Cu_3PS_4 as reported in our previous study.[18,23,24]

In this study, the electrochemical properties and Li storage mechanism of Ag_3PS_4 as cathode active material (CAM) were studied in SSBs with β-Li_3PS_4 as SE and In/InLi as anode. The composite cathode consists of Ag_3PS_4: β-Li_3PS_4: C65 = 40: 50: 10 wt%. The Ag_3PS_4 battery demonstrates an initial discharge capacity of 325 mAh g^{-1} at 10 mA g^{-1} and 60 °C, but the capacity continuously fades to 90 mAh g^{-1} after 100 cycles at 50 mA g^{-1}. Post-mortem characterization by XRD, XPS, and Raman spectroscopy revealed that while Ag_3PS_4 formation is initially partially reversible, it gradually irreversibly converts to a mixture of Ag_2S, S_8, and the polysulfides $Ag_2P_2S_6$ and $Li_2P_2S_6$ during cycling.

2. Electrochemical Measurements

The electrochemical properties of the SSBs (two-electrode geometry in all cases) were tested at 60 °C in a Binder MK(E4) chamber. The electrochemical performance was recorded using a Biologic BCS-805 system during galvanostatic cycling. For all cycling tests, the program contained precycling and long-term cycling steps.[18] The precycling program included three steps with different voltage windows of 1.0–2.8, 0.9–2.8, and 0.8–2.8 V. All precycling steps were performed at 10 mA g^{-1}. The precycling steps were performed in an effort to increase the utilization of active material. After the precycling procedure, the current was increased to 50 mA g^{-1} for long-term testing in a voltage range of 0.8–2.8 V. A similar precycling program was also applied prior to rate capability measurements, after which the battery was cycled for 5 cycles each at currents of 10, 20, 50, 100, 200, and 500 mA g^{-1} between 0.8 and 2.8 V, followed by returning the current to 10 mA g^{-1} for another 10 cycles. Cyclic voltammetry (CV) data were recorded at 1 mV s^{-1} between 0.18 and 2.18 V vs. Li^+/(In/InLi), corresponding to 0.80–2.80 V vs. Li^+/Li.[25] Electrochemical impedance spectroscopy (EIS) was recorded at open circuit voltage (OCV), lithiated (0.8 V), and delithiated (2.8 V) states with an SP-200 system from BioLogic with a 20 mV excitation voltage from 3 MHz to 0.1 Hz. To measure the Ag^+ conductivity of Ag_3PS_4, EIS measurements were performed from 1 MHz to 0.1 Hz on a battery composed of SS/Ag_3PS_4/SS (where SS is stainless steel). All acquired EIS data were fitted using the RelaxIS 3 (rhd instruments) software. The ionic conductivity was calculated according to Equation (2):

$$\sigma_{Ag+} = l/(R \times S) \quad (2)$$

where l is the thickness of the Ag_3PS_4 pellet, S is the area of the Ag_3PS_4 pellet, and R is the measured resistance.

3. Characterization

Phase identification of the prepared Ag_3PS_4 powder was determined by X-ray diffraction (XRD) in a Bruker D2 Phaser using a Cu Kα radiation source operating at 30 kV at 10 mA. Besides the prepared Ag_3PS_4, all other samples containing β-Li_3PS_4 were measured by covering the sample with a KAPTON-PI film to prevent air exposure. Scanning electron microscopy (SEM) and energy dispersive X-ray spectroscopy (EDX) were conducted with a Thermo Fisher Scientific Phenom Desktop SEM operating at 15 kV. All samples were prepared in an Ar-filled glovebox and quickly transferred into the vacuum chamber of the SEM for testing. Raman spectroscopy was conducted using a Renishaw inVia confocal Raman microscope with a 532 nm laser. Raman measurements were performed with 1% laser power and an exposure time of 30 s for 5 accumulations. To prevent air exposure to the sample, an airtight sample case with a CaF_2 window from Crystran Ltd. was employed. X-ray photoelectron spectroscopy (XPS) was performed on a JEOL JPS-9030 photoelectron spectrometer using monochromatic Al Kα radiation as the excitation source ($h\nu = 1486.6$ eV). Surface etching was conducted using Ar^+ bombardment with a bias voltage of 300 V for 50 min. To protect the samples from air exposure, all XPS samples were prepared in an Ar-filled glovebox and transferred using an air-tight sample transfer system.

4. Results and Discussion

Figure 1a shows an XRD pattern of the synthesized product with an orange color (see inset). The orthorhombic structure (Pmn21) aligns well with the Ag_3PS_4 reference pattern (ICSD 98-041-6585), but the sample exhibits broadened peaks indicating the small crystallite sizes. The surface of the synthesized Ag_3PS_4 was found to be rough, but with a uniform elemental distribution of Ag, P, and S, as shown by the SEM and EDX images in Figure 1b. The Ag^+ conductivity of the Ag_3PS_4 was measured to be 2.25×10^{-4} S cm^{-1} (Figure 1c), which is comparable to the Li^+ conductivity of β-Li_3PS_4.[26]

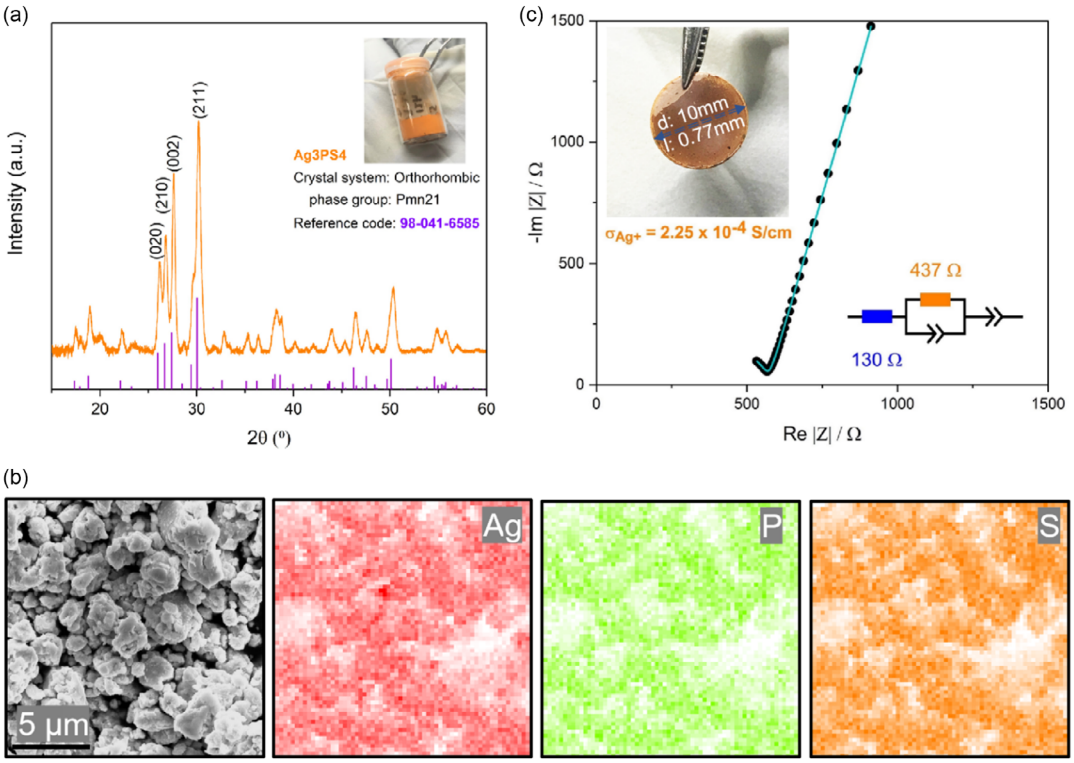

Figure 1. a) XRD pattern of the prepared Ag_3PS_4. The inset shows a picture of the synthesized Ag_3PS_4 powder product, while the purple reference lines are from ICSD 98-041-6585. b) SEM image and Ag, P, and S EDX mappings of the prepared Ag_3PS_4 powders. The scale bar is 5 µm. c) Nyquist plot (solid circuit) and the fitting result (green line) of an SS/Ag_3PS_4/SS (where SS is stainless steel) symmetric cell at room temperature. The insets show the equivalent circuit model and a photo of a pelletized sample after testing.

To test the electrochemical properties of Ag_3PS_4, a battery with Li as anode (Li/β-Li_3PS_4/(Ag_3PS_4: β–Li_3PS_4: C65 = 40: 50: 10 wt%)) was prepared and cycled between 0.1 and 2.8 V vs. Li^+/Li at 10 mA g^{-1} at 60 °C. Assuming a theoretical specific capacity of 610 mAh g^{-1}, the theoretical areal capacity of the electrode is 2.44 mAh cm^{-2}. The voltage profile and obtained capacity are shown in **Figure 2**a. Capacity values at 0.80 and 0.62 V are highlighted as they correspond to the lower cutoff voltage and the theoretical lithiation limit in the subsequent tests when using an In/InLi anode. The region between 0.8 and 0.62 V shows a sloping voltage behavior indicating that no additional phase transformation takes place in this area. The graph also shows that the discharge capacity is higher than the theoretical capacity of the Ag_3PS_4 alone, which is likely caused by some additional side reactions of the β-Li_3PS_4 SE. As it is well known that the use of Li metal can cause dendrites and that the Li/β-Li_3PS_4 interface is unstable,[15,27] subsequent tests were performed using In/InLi as anode with a cutoff voltage of 0.8 V vs. Li^+/Li during cycling.[8,9] The capacity was calculated based on the weight of Ag_3PS_4, the voltage was calibrated by taking Li as the reference electrode, and all electrochemical tests were conducted at 60 °C. To improve the utilization of Ag_3PS_4 in the electrochemical reaction, a precycling procedure with sequentially widening voltage windows was applied at 10 mA g^{-1}, see ref. [18,28] and experimental section.

Along with an increase of the discharge capacity from 216 to 325 mAh g^{-1}, the voltage profiles also changed when the lower cutoff voltage decreased from 1.0 to 0.8 V during precycling, as shown in Figure 2b. After increasing the current from 10 to 50 mA g^{-1}, the cell lost 19% of its discharge capacity, falling from 325 to 262 mAh g^{-1}. The SSB also suffers a continuous capacity fade during cycling at 50 mA g^{-1} (see Figure 2c), reaching 91 mAh g^{-1} after 100 cycles. Over 100 cycles at 50 mA g^{-1}, the average coulomb efficiency (CE) of the cell is 97.0%, corresponding to an average loss of 1.7 mAh g^{-1} per cycle.

Considering the working voltage window over the electrochemical stability window of β-Li_3PS_4, the capacity contribution of side reactions was estimated by the electrochemical performance of the SSB without CAM (β-Li_3PS_4: C65 = 3: 1 by weight) in our previous Cu_3PS_4 work.[18] Counting the cathode composition ratio of Ag_3PS_4: β-Li_3PS_4: C65 = 40: 50: 10 wt% in the cathode, side reactions contribute around 3.5 mAh g^{-1}[Ag_3PS_4] during cycling. While we cannot exclude some excess capacity due to side reactions with the SE, the contribution is likely negligible.

Cyclic voltammetry (CV) provides a better view of the redox activity evolution of the battery than the voltage profiles shown in Figure 2b. As shown in Figure 2d, five signals can be found, including two pairs of cathodic and anodic peaks located around 2.3 V (I, cathodic), 1.9 V (II, cathodic), 2.2 V (IV, anodic), and 2.4 V (V, anodic) along with a broad peak (III, cathodic) showing up from 1.1 to 0.8 V. Peaks I and V increase in intensity during cycling, while peaks II and IV show a decrease in their intensities during cycling. The cathodic peaks can be

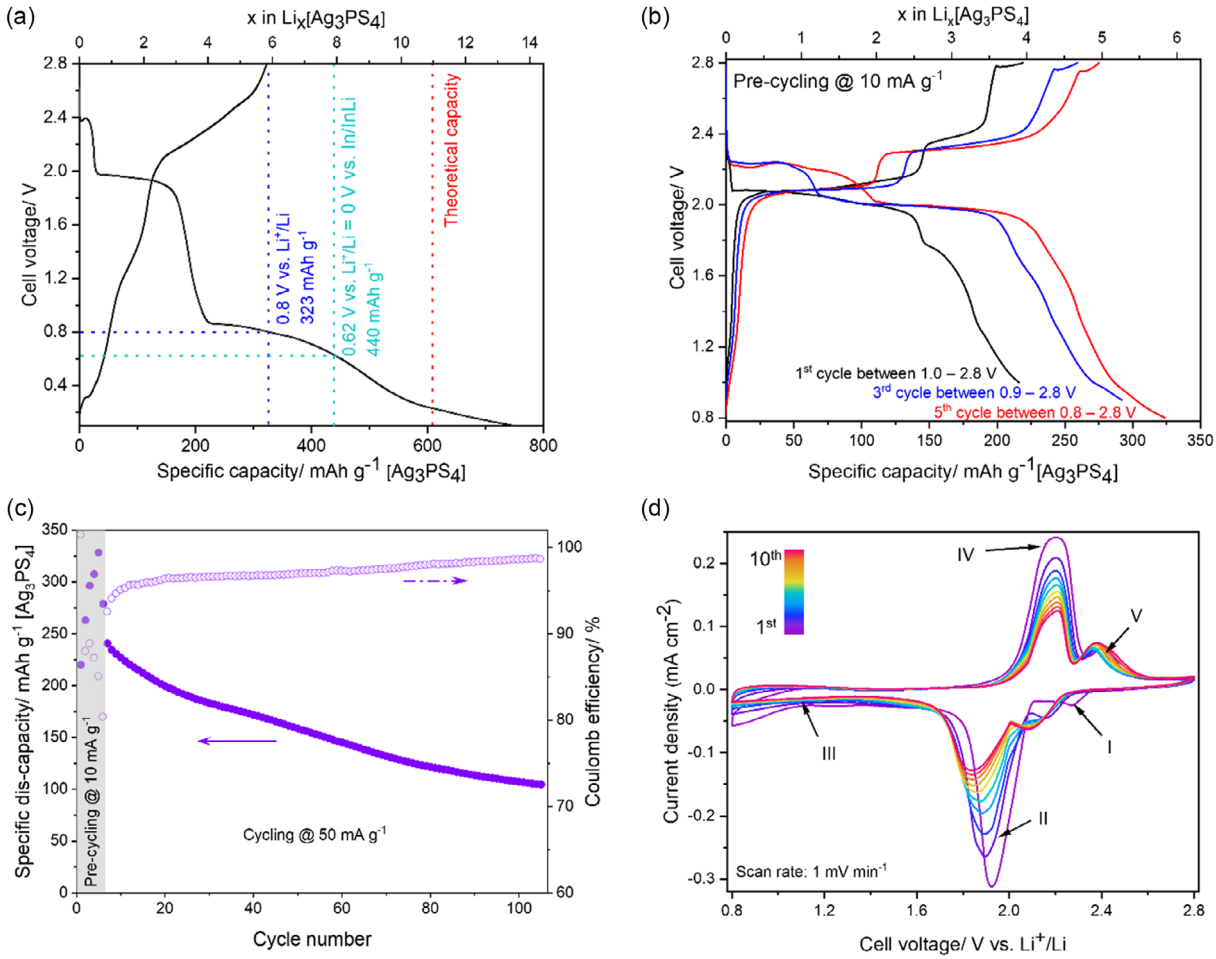

Figure 2. Electrochemical behavior of the Ag_3PS_4 SSBs at 60 °C. a) The 1st cycle voltage profile of a SSB with Ag_3PS_4 as CAM, Li as anode and β-Li_3PS_4 as SE cycled at 10 mA g^{-1} between 0.1 and 2.8 V vs. Li$^+$/Li. b) Voltage profiles of Ag_3PS_4 SSBs during a precycling at 10 mA g^{-1} between 1.0–2.8 V (black, the 1st cycle), 0.9–2.8 V (blue, the 3rd cycle), and 0.8–2.8 V (red, the 5th cycle) vs. Li$^+$/Li. c) The cycling stability and Coulomb efficiency over 105 cycles. d) Cyclic voltammetry of the SSBs at a scan rate of 1 mV min^{-1}. The first 10 cycles were measured and, with cycle numbers shown in the color bar. Measurements shown in b, c, and d were conducted with an In/InLi anode.

observed to continuously shift to lower voltages during cycling, but no similar drift can be found for the anodic peaks. Such a behavior indicates a gradual change of the electrochemically active materials or structural changes that occur during cycling.[29,30] While we do not currently have a full understanding of this behavior in the tested cells, we hypothesize that this may be related to differences in conductivity of the electrode at specific states of charge.[31]

To gain insight into the structural evolution during cycling, XRD patterns were collected ex-situ from electrodes at OCV and at different states of charge, as shown in **Figure 3**a. After hand grinding, the prepared cathode shows the expected signals from both Ag_3PS_4 and β-Li_3PS_4 (although their peaks are rather broad and overlap significantly in the region between 25° and 30° 2θ). When the cell is discharged to 2.0 V, the Ag_3PS_4 is found to partially convert to Ag_2S (i.e., the (1 2 1) and (1 2 $\bar{2}$) reflections at 34.4° and 36.8° 2θ, respectively) and Ag (i.e., the (1 1 1) reflection at 38.0° 2θ) along with other possible side products such as $Ag_2P_2S_6$ (i.e., the (2 2 0) reflection at 32.4° 2θ) and $Li_2P_2S_6$ (i.e., the (2 2 0) and (3 1 $\bar{2}$) reflections at 32.3° and 31.9° 2θ, respectively). With further discharge to 0.8 V, signals attributed to Ag_3PS_4, $Ag_2P_2S_6$, Ag_2S, and $Li_2P_2S_6$ get diminished but are still distinguishable. Meanwhile, strong Ag peaks and weak Li_2S (i.e., the (1 1 1) and (2 2 0) reflections at 25.9° and 43.0° 2θ, respectively) signals become visible, showing that Ag_3PS_4 is reduced upon discharge, in line with the reaction presented in Equation (1). The weak Li_2S signal intensity indicates that Li_2S may be amorphous, which would be consistent with what is generally observed for conversion reactions.[32] The presence of Li_2S in the discharged to 0.8 V sample is further supported by Raman measurements (Figure S1 in the Supporting Information), where a signal that is characteristic of the T_{2g} phonon mode of Li_2S can be found at 370 cm^{-1}.[33] The Raman signals at 421 and 370 cm^{-1} also support the formation of $Li_2P_2S_6$ after lithiation.[34] During charging, at a state of 2.2 V, the peak intensity corresponding to Ag_3PS_4 and Ag_2S is observed to again increase in concert with a decrease in the Ag and Li_2S signals. Further charging to 2.8 V shows the complete

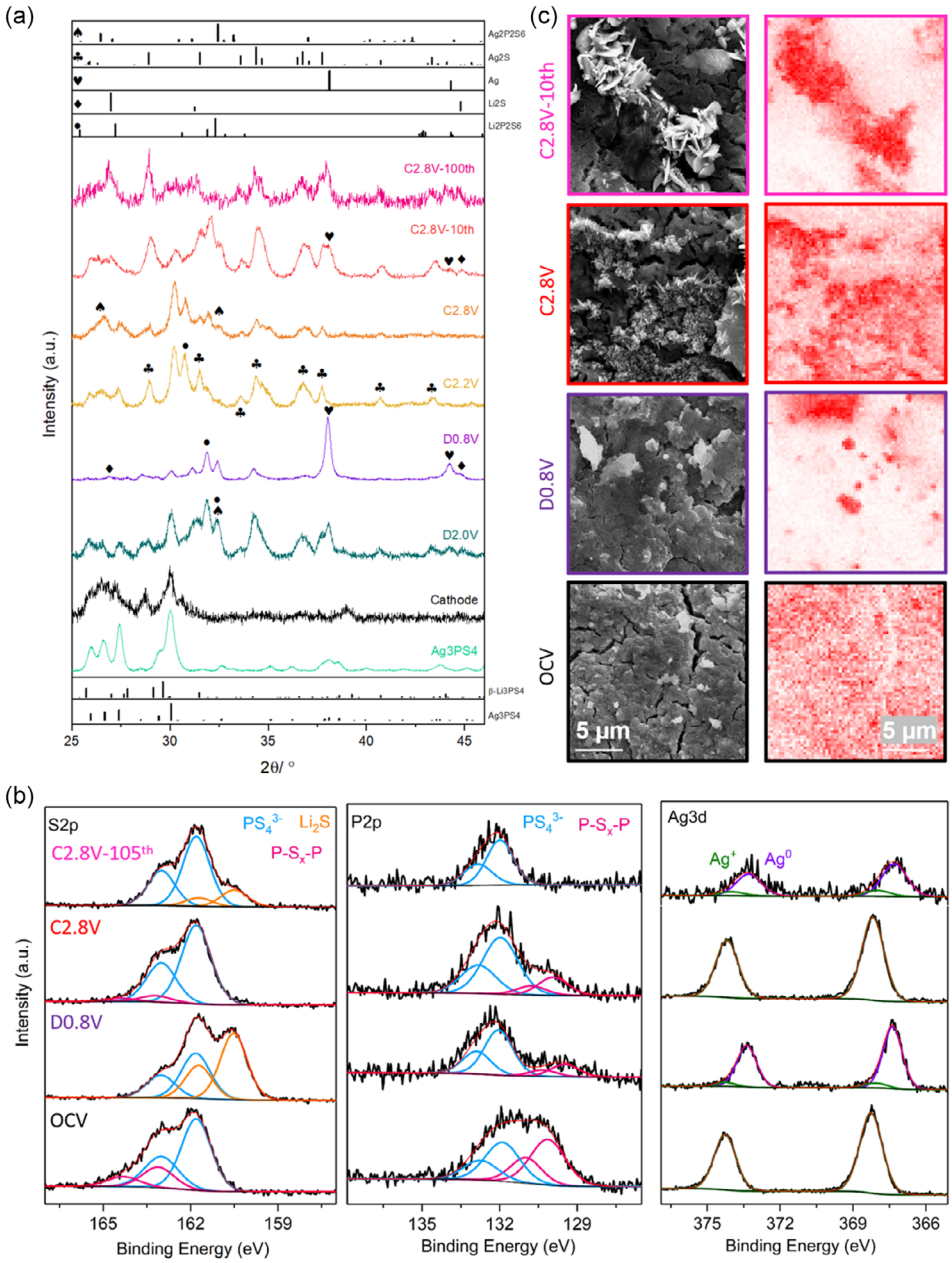

Figure 3. Postmortem measurements of the SSBs. a) Ex situ XRD patterns of Ag_3PS_4, the prepared cathodes, 1st Dis-2.0 V, 1st Dis-0.8 V, 1st Char-2.2 V, 1st Char-2.8 V, 10th Char-2.8 V, and 105th Char-2.8 V. Except for Li_2S, whose reference pattern is from ICDD, all other reference patterns are from ICSD: Ag (98-004-4387), Li_2S (98-006-0432), Ag_2S_1 (98-003-0445), $Ag_2P_2S_6$ (98-003-0531), and $Li_2P_2S_6$ (253894). b) Bulk S2p, P2p, and Ag3d XPS spectra of the OCV, 1st Dis-0.8 V, 1st Char-2.8 V, and 105th Char-2.8 V electrochemical states, (from bottom to top). The bulk XPS data were collected after 1200s etching at 300 W. c) SEM and the corresponding Ag EDX images of the cathode before reaction, the electrodes at the 1st Dis-0.8 V, 1st Char-2.8 V, and 10th Char-2.8 V states. The scale bar is 5 µm.

disappearance of Ag and Li_2S and a decrease of Ag_2S alongside a concomitant increase in Ag_3PS_4, $Ag_2P_2S_6$, and $Li_2P_2S_6$ in the electrode. A comparison of the 1st and 10th cycles at a state of charge of 2.8 V shows that the Ag_3PS_4 signals become weaker overall during the first 10 cycles, while the Ag_2S, $Ag_2P_2S_6$, and $Li_2P_2S_6$ peaks became more prominent. However, the signal intensities arising from Ag_3PS_4, $Ag_2P_2S_6$, and $Li_2P_2S_6$ are found to subsequently diminish in the following cycles, with only Ag_2S, Ag, and Li_2S becoming detectable after 105 cycles. This suggests that the $Ag_2P_2S_6$ and $Li_2P_2S_6$ undergo a process of growth followed by fading during cycling. At the same time, the relatively high intensity of Ag and Li_2S signals in the charged electrode (2.8 V) after 10 and 105 cycles indicates a deterioration of the reversibility of the reaction, possibly due to particle isolation within the cathode. During the initial charging process, there is an unidentified XRD signal that arises at 30.8° (2θ) (marked

with a question mark in Figure 3a), which is no longer visible after 10 and 105 cycles. At the same time, all XRD signals are relatively broad after cycling, indicating the presence of materials with a low degree of crystallinity in the electrode.

To better assign the possible existing products formed in the electrode at different states of charge, XPS and Raman spectroscopy were carried out to complement the XRD results. All XPS spectra were calibrated to the S $2p_{3/2}$ signal of the $[PS_4]^{3-}$ tetrahedra in β-Li_3PS_4 at 161.8 eV. All samples were etched (see details in the Experimental section) in order to obtain information from the bulk region as shown in Figure 3b. At OCV, two species can be found in the S 2p spectrum. One species has a doublet peaks of S $2p_{3/2}$ and S $2p_{3/2}$ with the binding energy (BE) of 161.8 and 163.2 eV, respectively, which is accordingly assigned to the PS_4^{3-} tetrahedra of β-Li_3PS_4 and Ag_3PS_4, as corroborated by the corresponding doublet P 2p peaks located at 132.2 eV (P $2p_{3/2}$) and 133.0 eV (P $2p_{1/2}$).[35] The second species at OCV has an S $2p_{3/2}$ BE of 163.3 eV and P $2p_{3/2}$ BE of 130.1 eV and is attributed to polysulfides with P-$[S]_n$-P structure. This is also evidenced by the broad Raman signal near 421 cm^{-1}, which may result from the convolution of signals arising from species related to $P_2S_7^{4-}$ (404 cm^{-1}), $P_2S_6^{4-}$ (393 cm^{-1}), and/or PS_3^{3-} (430 cm^{-1}),[36–38] as shown in Figure S1 (Supporting Information). These P–$[S]_n$–P structural motifs may result from fracturing of the PS_4^{3-} from Ag_3PS_4 and β-Li_3PS_4 due to the processing in this work and relate to the broadening of XRD signals observed in Figure 3a.[39–46] The P–$[S]_n$–P structural motifs are abbreviated as PS in the following text. The Ag 3d spectra indicate the presence of only Ag^+ at OCV with the Ag $3d_{5/2}$ and Ag $3d_{3/2}$ doublet peaks located at 368.2 and 374.2 eV, respectively, which is anticipated from the Ag_3PS_4 active material. When the samples are lithiated, corresponding to a state of charge of 0.8 V, most of the silver is found to reduce to Ag^0, with the $Ag3d_{5/2}$ feature shifting to 367.4 eV. It can also be found that part of silver remains as Ag^+ in the fully lithiated state, which can be attributed to the residual $Ag_2P_2S_6$ as observed in the XRD pattern. At the same time, Li_2S can be observed according to the appearance of the S $2p_{3/2}$ signal at 160.5 eV, which is also supported by the appearance of the T_{2g} Raman signal of Li_2S around 370 cm^{-1} in Figure S1 (Supporting Information).[47] There is also a significant reduction in the intensity of the PS motifs (see S2p and P2p spectra in Figure 3b) and a shift of the P$2p_{3/2}$ signal to a lower BE of 130.1 eV in the P2p spectrum, which is in line with the decreasing $Li_2P_2S_6$/ $Ag_2P_2S_6$ XRD intensities (Figure 3a) from the Dis-2.0 V to Dis-0.8 V samples, and indicates the development of other possible PS-containing compounds.[34,48] Note that there is no indication of the production of Li_3P according to XPS, which would be expected to show up in the P2p spectrum of the fully lithiated material around 126 eV if the conversion reaction goes to completion (see Equation (1)).[49] Instead, an additional doublet at 128.7 eV is found which might be attributed to other phosphorous-rich polyphosphide compounds such as LiP, LiP_5, or LiP_7.[50–52] Upon subsequent charging to 2.8 V, the reduced silver reversibly oxidizes back to Ag^+ and the compounds with PS motifs show up again in the delithiated electrode. According to XRD, at 2.8 V, the Ag^+ is expected to arise from a combination of Ag_2S, Ag_3PS_4, and $Ag_2P_2S_6$. The S $2p_{3/2}$ feature of Ag_2S is expected to be located at a similar BE to that of the PS_4^{3-} tetrahedra, making it difficult to distinguish the presence of this species by XPS alone. In line with the disappearance of the $Li_2P_2S_6$/$Ag_2P_2S_6$ signals observed in the electrode after 105 cycles via XRD, we found that the XPS spectra at 2.8 V after 105 cycles most closely resembles that of the cathode in the 1st fully lithiated state. Besides a large amount of Ag^0 and Li_2S, Ag_3PS_4, and PS motifs are no longer observable in the electrode after long-term cycling, indicating that the formed products (Ag^0 and Li_2S) become electrochemically isolated after many cycles and limit the reversibility of the Ag_3PS_4 and PS motifs ($Ag_2P_2S_6$, $Li_2P_2S_6$, etc.). Similar with our recent work on Cu_3PS_4, elemental sulfur is not observable in the delithiated (Char-2.8 V) sample by XPS due to the sublimation of sulfur under UHV conditions.[53] To support the conclusions from XPS measurements and evaluate the presence of additional species that may be lost to vacuum, Raman spectroscopy was conducted as well. The presence of S_8 [Raman shift: 153 cm^{-1} (asymmetric S-S bending), 220 cm^{-1} (symmetric S-S bending), 473 cm^{-1} (S—S bond stretching of the S_8 ring structure)[54]] in the delithiated sample after 10 cycles,[55] as shown in Figure S1 (Supporting Information).

SEM/EDX was used to determine variations in the electrode morphology during cycling. One intriguing observation is that many regular, planar particles appear in the charged samples, and these particles grew after cycling (Figure 3c). The EDX mappings in Figure 3c indicate that these planar particles are rich in Ag, which we therefore ascribed to the formation of planar shaped Ag_2S,[56] which we observed to increase after 10 cycles by XRD. Meanwhile, the silver ion conductivity of Ag_2S also promotes the continuous growth of silver-rich clusters.[41,55]

Overall, the XPS results unveil that the Ag_3PS_4 and PS motifs are initially converted to a combination of Ag, Li_2S, and reduced-PS species after discharge. Although the silver redox reaction exhibits reversibility in the beginning, we discovered that this reversibility gradually degrades during subsequent cycles. In line with the intense Ag XRD signal, the XPS results also found that most of the Ag–containing materials are converted to metallic Ag after cycling.

In situ EIS is a powerful tool to investigate the influence of composition and structural changes in SSBs through analyzing the variations in resistance during cycling. Based on differences in the equivalent circuit models for the fittings of the EIS data at OCV, lithiated, and delithiated states (see insets in **Figure 4**a–c), the EIS data were separated to follow their evolution, as shown in Figure 4d,e. The high-frequency semicircle (>33 kHz) corresponds to the bulk and grain boundary resistance of the SE, which gradually increases during the first 10 cycles. Along with the volume expansion of Ag_3PS_4 during lithiation, which is favorable for increasing the electrode pellet density, metallic Ag also forms in the electrode. Therefore, the electronic conductivity of the electrode after discharge is expected to display lower resistance than the corresponding delithiated states, as shown in the Bode plot in Figure S2 (Supporting Information).[57] The medium-frequency region contains overlapping contributions from different sources such as charge transfer and the cathode/anode interfaces.[58,59] All acquired Nyquist plots between 33 kHz and 0.88 Hz can be separated into two parts by the 36 Hz point, as marked by the highlighted middle points in Figure 4d,e. The periodic impedance behavior during cycling can be clearly seen from Figure 4f, showing the log Z-value at

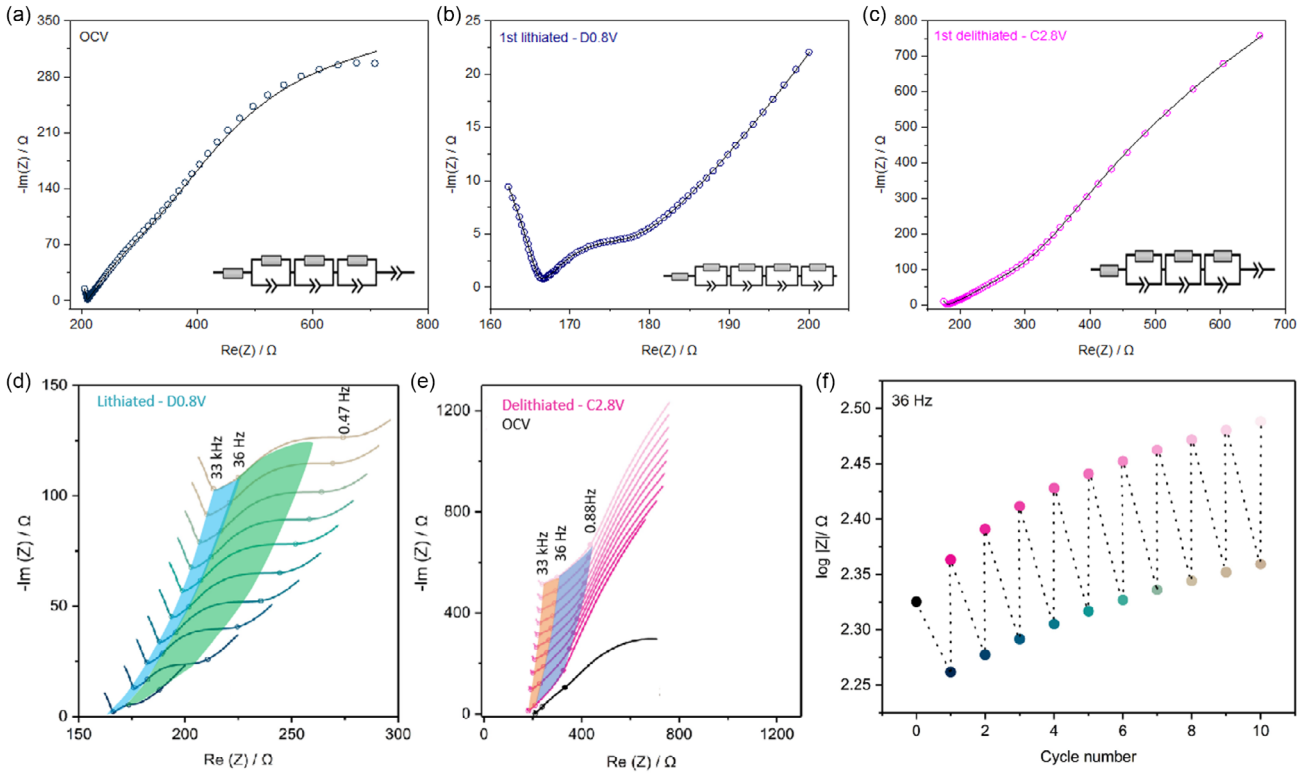

Figure 4. XPS spectra of the bulk electrode. a–c) EIS (solid points) together with the equivalent circuit model and the fitting curve (line) of the SSB at OCV, 1st lithiated, and 1st delithiated states. d–e) Evolution of the impedance of the lithiation (d), delithiation (red in e), and OCV (black in e) states during cycling at 60 °C. Note the different scaling for both plots with much larger resistance values in the delithiated state. The data corresponding to the medium-frequency range were separated into two parts by the points at 36 Hz. f) The evolution of the resistance values at 36 Hz during cycling. The in situ EIS measurements were conducted with In/InLi /β-Li_3PS_4 /Ag_3PS_4 SSBs in the frequency range of 3 MHz – 0.1 Hz under an exciation voltage of 20 mV.

36 Hz over 10 cycles. These conductivity changes may be the cause for the asymmetric evolution of the CV curve features observed in Figure 2d. In line with the XRD, XPS, and Raman spectra, the continuous impedance increase in the medium-frequency range further indicates a continuous deterioration of the SSBs during cycling. However, it should be considered that these experiments were conducted in two-electrode SSBs where all possible chemical and electrochemical behaviors become entangled and are therefore difficult to separate, making a more detailed and quantitative interpretation of the EIS data difficult.

5. Proposed Reaction Mechanism

Summarizing the previous results, we can propose a reaction mechanism for Ag_3PS_4 with lithium. Initial lithiation from OCV to 2.0 V vs. Li^+/Li starts with the formation of Ag_2S and PS motifs like $Ag_2P_2S_6$ and $Li_2P_2S_6$. The appearance of metallic Ag at this stage indicates that Ag_3PS_4 experiences a different direct phase conversion reaction mechanism than the intercalation-conversion reaction mechanism reported for Cu_3PS_4.[18] It is important to note that $Li_2P_2S_6$ is known to be a poor ionic conductor (7.8×10^{-11} S cm^{-1} at room temperature),[60] which may result in Li consumption and reduced reversibility during cycling. When reaching 0.8 V vs. Li^+/Li, most of the Ag_3PS_4 was converted to Ag and Li_2S, with residual Ag_2S, $Ag_2P_2S_6$, and $Li_2P_2S_6$ in the electrodes. Despite reforming Ag_3PS_4 during the first cycles, a mixture containing Ag_2S, S_8, PS motifs ($Ag_2P_2S_6$ and $Li_2P_2S_6$), and other compounds was observed during cycling. The evolving local structure and composition decreases the reversibility of the electrochemically reversible Ag_3PS_4 and PS motifs and finally results in capacity fading and the absence of XPS signals of Ag_3PS_4 and PS motifs after 105 cycles. In a nutshell, the Ag_3PS_4 reaction with lithium was partially reversible, but experienced a complex reaction mechanism and gradually lost its reversibility over cycling.

6. Conclusion

The lithiation mechanism and electrochemical properties of Ag_3PS_4 as electrode were investigated in lithium SSBs using β-Li_3PS_4 as SE. The pristine Ag_3PS_4 first converts to Ag_2S, Ag, and PS compounds such as $Ag_2P_2S_6$ and $Li_2P_2S_6$ at 2.0 V, then these compounds are further transformed into Ag and Li_2S after discharging to 0.8 V. When the lithium is subsequently extracted from the lithiated electrode, Ag_3PS_4 is found to reform in the

electrode, but with $Ag_2P_2S_6$ and $Li_2P_2S_6$ side products. The reversibility of Ag_3PS_4 during cycling gradually degrades, and Ag_2S and S_8 become the dominant active phases along with the formation and consumption of $Ag_2P_2S_6$ and $Li_2P_2S_6$ over cycling. Accompanied by the phase transformation of Ag_3PS_4 and phase segregation of Ag_2S and S_8, the structural changes are found to deteriorate the overall conductivity and therefore the electrochemical activity of the electrodes after many cycles. Overall, the conversion reaction of Ag_3PS_4 with Li under mechanical confinement in an SSB has been successfully demonstrated. While the reaction is partially reversible at the beginning, Ag_2S and S_8 become the redox active phases over cycling. A specific benefit of Ag_3PS_4 over other conversion electrodes is the relatively mild volume change (+49%) and the formation of conductive intermediate phases, which can support a better reversibility compared to other conversion reactions. On the other hand, further improvements are needed, as the overall properties (capacity, polarization, and reversibility) of the reaction lag behind those of other sulfide conversion CAMs such as CuS or Cu_3PS_4.

7. Experimental Section

Ag_3PS_4 was prepared by planetary ball milling stoichiometric amounts of Ag (Alfa-Aesar, 99.9%), S (Sigma-Aldrich, 99.5%), and P_2S_5 (Sigma-Aldrich, 99%) at 600 rpm for 12 h in a 45 mL ZrO_2 ball milling jar with a Fritsch Pulverisette-7 Micro Mill via periodically rotating for 30 min and resting for 5 min, the loading ratio of ZrO_2 balls (10 mm) to reagents was 10: 1 wt%. The acquired yellow/blackish intermediate powder became orange after heat treatment at 100 °C for 4 h in a Büchi glass oven. The β-Li_3PS_4 was provided by BASF. In and Li were obtained from Chempur and Rockwood Lithium, respectively, and electrodes were assembled as previously reported.[25]

All SSBs were assembled by the same procedure as reported in our previous work.[18] For making the batteries, 70 mg β-Li_3PS_4 was pelletized by uniaxial pressing in a 10 mm diameter polyether ether ketone mold, and then 10 mg of the desired cathode composite (Ag_3PS_4: β-Li_3PS_4: C65 = 40: 50: 10 wt%) was distributed over the β-Li_3PS_4 surface and again pressed at 3 tons (375 MPa) for 3 min using a YLJ-15 T Laboratory Press from MTI Corporation with a stainless steel piston. The battery was then closed after placing an In/InLi anode on the other side of the β-Li_3PS_4, with the molar ratio of indium and lithium being carefully controlled above 1. A static external pressure (≈8 MPa) was applied to the battery by using an Al frame to guarantee enough solid–solid contact in the battery.

Supporting Information

Supporting Information is available from the Wiley Online Library or from the author.

Acknowledgements

P.A. and K.A.M. acknowledge support from the project KAROFEST (grant no. 03XP0498A) funded by the Bundesministerium für Bildung und Forschung (BMBF). Z.G.Z. thanks the China Scholarship Council (CSC) for funding. Z.G.Z. and P.A. appreciate support for the materials synthesis from Wolfgang Brehm and discussion with Lukas Medenbach.

Open Access funding enabled and organized by Projekt DEAL.

Conflict of Interest

The authors declare no conflict of interest.

Data Availability Statement

The data that support the findings of this study are available from the corresponding author upon reasonable request.

Keywords

Ag_3PS_4, multielectron reaction, solid-state batteries, transition-metal thiophosphate

Received: May 22, 2024
Revised: June 25, 2024
Published online: July 27, 2024

[1] Z. Zhang, Y. Shao, B. Lotsch, Y.-S. Hu, H. Li, J. Janek, L. F. Nazar, C.-W. Nan, J. Maier, M. Armand, L. Chen, *Energy Environ. Sci.* **2018**, *11*, 1945.
[2] T. Famprikis, P. Canepa, J. A. Dawson, M. S. Islam, C. Masquelier, *Nat. Mater.* **2019**, *18*, 1278.
[3] X. Xu, Y. Liu, O. O. Kapitanova, Z. Song, J. Sun, S. Xiong, *Adv. Mater.* **2022**, *34*, 2207232.
[4] A. Manthiram, X. Yu, S. Wang, *Nat. Rev. Mater.* **2017**, *2*, 16103.
[5] M. L. Yang, Y. Yao, M. Y. Chang, F. L. Tian, W. R. Xie, X. L. Zhao, Y. Yu, X. Y. Yao, *Adv. Energy Mater.* **2023**, *13*, 2300962.
[6] N. Wang, M. Y. Chang, W. R. Xie, G. Z. Liu, H. He, X. Y. Yao, *Nanoscale* **2024**, *16*, 8915.
[7] G. F. Dewald, S. Ohno, M. A. Kraft, R. Koerver, P. Till, N. M. Vargas-Barbosa, J. Janek, W. G. Zeier, *Chem. Mater.* **2019**, *31*, 8328.
[8] F. Han, T. Gao, Y. Zhu, K. J. Gaskell, C. Wang, *Adv. Mater.* **2015**, *27*, 3473.
[9] T. Swamy, X. Chen, Y.-M. Chiang, *Chem. Mater.* **2019**, *31*, 707.
[10] S. Ohno, C. Rosenbach, G. F. Dewald, J. Janek, W. G. Zeier, *Adv. Funct. Mater.* **2021**, *31*, 2010620.
[11] R. Koerver, F. Walther, I. Aygün, J. Sann, C. Dietrich, W. G. Zeier, J. Janek, *J. Mater. Chem.* **2017**, *5*, 22750.
[12] T. Hakari, M. Nagao, A. Hayashi, M. Tatsumisago, *J. Power Sources* **2015**, *293*, 721.
[13] T. K. Schwietert, V. A. Arszelewska, C. Wang, C. Yu, A. Vasileiadis, N. J. J. de Klerk, J. Hageman, T. Hupfer, I. Kerkamm, Y. Xu, E. van der Maas, E. M. Kelder, S. Ganapathy, M. Wagemaker, *Nat. Mater.* **2020**, *19*, 428.
[14] D. H. S. Tan, E. A. Wu, H. Nguyen, Z. Chen, M. A. T. Marple, J.-M. Doux, X. Wang, H. Yang, A. Banerjee, Y. S. Meng, *ACS Energy Lett.* **2019**, *4*, 2418.
[15] W. D. Richards, L. J. Miara, Y. Wang, J. C. Kim, G. Ceder, *Chem. Mater.* **2016**, *28*, 266.
[16] Y. Fujii, A. Miura, N. C. Rosero-Navarro, M. Higuchi, K. Tadanaga, *Electrochim. Acta* **2017**, *241*, 370.
[17] W. Brehm, A. L. Santhosha, Z. Zhang, C. Neumann, A. Turchanin, A. Martin, N. Pinna, M. Seyring, M. Rettenmayr, J. R. Buchheim, P. Adelhelm, *Adv. Funct. Mater.* **2020**, *30*, 1910583.

[18] Z. Zhang, K. A. Mazzio, L. M. Riegger, W. Brehm, J. Janek, J. Sann, P. Adelhelm, Copper Thiophosphate, *Energy Technol.* **2023**, *11*, 2300553.
[19] Z. M. Xu, S. H. Bo, H. Zhu, *ACS Appl. Mater. Interfaces* **2018**, *10*, 36941.
[20] Y. Fujii, A. Miura, N. C. Rosero-Navarro, Y. Mizuguchi, C. Moriyoshi, Y. Kuroiwa, M. Higuchi, K. Tadanaga, *J. Electrochem. Soc.* **2018**, *165*, A2948.
[21] A. Qiao, H. Tao, Y. Yue, *J. Non Cryst. Solids* **2019**, *521*, 119476.
[22] C.-M. Park, H. Jung, H.-J. Sohn, *Electrochem. Solid-State Lett.* **2009**, *12*, A171.
[23] M. M. El-Nahass, A. A. M. Farag, E. M. Ibrahim, S. Abd-El-Rahman, *Vacuum* **2004**, *72*, 453.
[24] D. Karashanova, N. Starbov, *Appl. Surf. Sci.* **2006**, *252*, 3011.
[25] A. L. Santhosha, L. Medenbach, J. R. Buchheim, P. Adelhelm, *Batter. Supercaps* **2019**, *2*, 524.
[26] Z. Liu, W. Fu, E. A. Payzant, X. Yu, Z. Wu, N. J. Dudney, J. Kiggans, K. Hong, A. J. Rondinone, C. Liang, *J. Am. Chem. Soc.* **2013**, *135*, 975.
[27] M. Sun, T. Liu, Y. Yuan, M. Ling, N. Xu, Y. Liu, L. Yan, H. Li, C. Liu, Y. Lu, Y. Shi, Y. He, Y. Guo, X. Tao, C. Liang, J. Lu, *ACS Energy Lett.* **2021**, *6*, 451.
[28] T. Takeuchi, H. Kageyama, K. Nakanishi, M. Ogawa, T. Ohta, A. Sakuda, H. Sakaebe, H. Kobayashi, Z. Ogumi, *J. Electrochem. Soc.* **2015**, *162*, A1745.
[29] R. Koerver, I. Aygün, T. Leichtweiß, C. Dietrich, W. Zhang, J. O. Binder, P. Hartmann, W. G. Zeier, J. Janek, *Chem. Mater.* **2017**, *29*, 5574.
[30] Z. Zhang, K. Dong, K. A. Mazzio, A. Hilger, H. Markötter, F. Wilde, T. Heinemann, I. Manke, P. Adelhelm, *Adv. Energy Mater.* **2023**, *13*, 2203143.
[31] J. Yang, B. Yan, J. Ye, X. Li, Y. Liu, H. You, *Phys. Chem. Chem. Phys.* **2014**, *16*, 2882.
[32] F. Klein, B. Jache, A. Bhide, P. Adelhelm, *Phys. Chem. Chem. Phys.* **2013**, *15*, 15876.
[33] B. Bertheville, H. Bill, H. Hagemann, *J. Phys.: Condens. Matter* **1998**, *10*, 2155.
[34] F. M. Delnick, G. Yang, E. C. Self, H. M. Meyer III, J. Nanda, *J. Phys. Chem. C* **2020**, *124*, 27396.
[35] C. Dietrich, D. A. Weber, S. J. Sedlmaier, S. Indris, S. P. Culver, D. Walter, J. Janek, W. G. Zeier, *J. Mater. Chem. A* **2017**, *5*, 18111.
[36] B. Fan, Q. Zhang, Z. Luo, X. Zhang, H. Ma, P. Fan, B. Xue, *Solid State Ion* **2019**, *343*, 115073.
[37] R. Zhao, S. Kmiec, G. Hu, S. W. Martin, *ACS Appl. Mater. Interfaces* **2020**, *12*, 2327.
[38] H. Yao, K. Yan, W. Li, G. Zheng, D. Kong, Z. W. Seh, V. K. Narasimhan, Z. Liang, Y. Cui, *Energy Environ. Sci.* **2014**, *7*, 3381.
[39] M. Hagen, P. Schiffels, M. Hammer, S. Dörfler, J. Tübke, M. J. Hoffmann, H. Althues, S. Kaskel, *J. Electrochem. Soc.* **2013**, *160*, A1205.
[40] E. Nagai, T. S. Arthur, P. Bonnick, K. Suto, J. Muldoon, *MRS Adv.* **2019**, *4*, 2627.
[41] O. Alekperov, Z. Jahangirli, R. Paucar, *Phys. Status Solidi B* **2016**, *253*, 2049.
[42] J. Hannauer, J. Scheers, J. Fullenwarth, B. Fraisse, L. Stievano, P. Johansson, *Chemphyschem* **2015**, *16*, 2755.
[43] Y. Aoki, K. Ogawa, T. Nakagawa, Y. Hasegawa, Y. Sakiyama, T. Kojima, M. Tabuchi, *Solid State Ion* **2017**, *310*, 50.
[44] J. Sun, Y. Sun, M. Pasta, G. Zhou, Y. Li, W. Liu, F. Xiong, Y. Cui, *Adv. Mater.* **2016**, *28*, 9797.
[45] P. Toffoli, P. Khodadad, N. Rodier, *Acta Crystallogr.* **1977**, *33*, 1492.
[46] Z. W. Seh, H. Wang, P.-C. Hsu, Q. Zhang, W. Li, G. Zheng, H. Yao, Y. Cui, *Energy Environ. Sci.* **2014**, *7*, 672.
[47] C. Dietrich, R. Koerver, M. W. Gaultois, G. Kieslich, G. Cibin, J. Janek, W. G. Zeier, *Phys. Chem. Chem. Phys.* **2018**, *20*, 20088.
[48] A. Kato, H. Kowada, M. Deguchi, C. Hotehama, A. Hayashi, M. Tatsumisago, *Solid State Ion* **2018**, *322*, 1.
[49] K. N. Wood, K. X. Steirer, S. E. Hafner, C. Ban, S. Santhanagopalan, S.-H. Lee, G. Teeter, *Nat. Commun.* **2018**, *9*, 2490.
[50] K. N. Wood, G. Teeter, *ACS Appl. Energy Mater.* **2018**, *1*, 4493.
[51] S. Wenzel, S. J. Sedlmaier, C. Dietrich, W. G. Zeier, J. Janek, *Solid State Ion* **2018**, *318*, 102.
[52] Y. Xu, Y. Liu, Y. Zhu, S. Zheng, Y. Liu, C. Luo, K. Gaskell, B. Eichhorn, C. Wang, Stabilized sulfur as cathodes for room temperature sodium-ion batteries. No. SAND2013-4397J. Sandia National Lab.(SNL-NM), Albuquerque, NM (United States); University of Maryland, College Park, MD (United States), **2013**.
[53] C. Nims, B. Cron, M. Wetherington, J. Macalady, J. Cosmidis, *Sci. Rep.* **2019**, *9*, 7971.
[54] L. Medenbach, I. Escher, N. Köwitsch, M. Armbrüster, L. Zedler, B. Dietzek, P. Adelhelm, *Angew. Chem., Int. Ed.* **2018**, *57*, 13666.
[55] W. Hao, H. Si, X. Cheng, W. Zhu, X. Qiu, *Solid State Ion* **2019**, *340*, 115015.
[56] T. Ohtomo, A. Hayashi, M. Tatsumisago, Y. Tsuchida, S. Hama, K. Kawamoto, *J. Power Sources* **2013**, *233*, 231.
[57] M. Yamamoto, M. Takahashi, Y. Terauchi, Y. Kobayashi, S. Ikeda, A. Sakuda, *J. Ceram. Soc. Jpn.* **2017**, *125*, 391.
[58] T. Shi, Y.-Q. Zhang, Q. Tu, Y. Wang, M. C. Scott, G. Ceder, *J. Mater. Chem. A* **2020**, *8*, 17399.
[59] C. Dietrich, D. A. Weber, S. Culver, A. Senyshyn, S. J. Sedlmaier, S. Indris, J. Janek, W. G. Zeier, *Inorg. Chem.* **2017**, *56*, 6681.
[60] Ö.U. Kudu, T. Famprikis, B. Fleutot, M.-D. Braida, T. Le Mercier, M. S. Islam, C. Masquelier, *J. Power Sources* **2018**, *407*, 31.